Petrography and Major Element Geochemistry of the Endengue Iron Formations, Ntem Complex, South Cameroon

Robinson Tchatchueng[1,*], Habib Dadjo Djamo[2], Timoléon Ngnotué[1], Evine Laure Tanko Njiosseu[1], Mamadou Traoré[3], Cyriel Moudioh[4], Hervé Wabo[5], Cédric Djeutchou[5], Jean Paul Nzenti[4]

[1]Department of Earth Sciences, University of Dschang, P.O. Box 67 Dschang, Cameroon
[2]Institute for Geological and Mining Research, P.O. Box 4110 Yaounde-Cameroon
[3]University of Çukurova, Department of Geological Engineering, Sarıçam, Adana, Turkey
[4]Department of Earth Sciences, University of Yaoundé I, P.O. Box 812 Yaoundé
[5]Department of Geology University of Johannesburg-South Africa, P.O. Box: 524 Auckland Park 2006 Gauteng APK Campus
*Corresponding author: tchatchuengrobinson@yahoo.com

Abstract The Endengue iron formations (IFs) belong to the Archaen Ntem greenstones belt at the NW edge of Congo craton and comprise magnetite-bearing gneiss associated with biotite-pyroxene gneiss and intruded by biotite granite and charnockite. The studied IFs are fine-grained; weak foliated rocks, composed of quartz-pyroxene-magnetite-plagioclase mineral assemblages, suggesting high-grade metamorphism. Whole-rock geochemical composition reveals that iron and silica are the main chemical components of the studied IFs with an average $\sum TFe_2O_3 + SiO_2$ of 93.06 wt-%, suggesting the purity of the chemical precipitation. In addition, the high average Si/Al (38.69); Fe/Ti (766.83) and Fe/Al (56.36) ratios and the Fe/Ti vs Al/(Al+Fe+Mn) plot suggest that the major components (> 80%) of the Endengue IFs are predominantly hydrothermal in origin. However, the slightly high $Al_2O_3+TiO_2$ content (average of 2.14 wt-%) suggested a detrital input during their deposition. The studied IF samples with an average Total Fe content of 39.40 wt-%, low gangue (34.68 wt-% SiO_2 and 1.05 wt-% Al_2O_3) and deleterious (P_2O_5: 0.07 wt-%) elements contents, correspond to accepted commercial low grade siliceous ore by global standards. The Edengue IFs shared chemical similarities with other Precambrian IFs worldwide.

Keywords: *iron formation, chemical precipitation, hydrothermal origin, low grade siliceous ore, Ntem complex, southern Cameroon*

Cite This Article: Robinson Tchatchueng, Habib Dadjo Djamo, Timoléon Ngnotué, Evine Laure Tanko Njiosseu, Mamadou Traoré, Cyriel Moudioh, Hervé Wabo, Cédric Djeutchou, and Jean Paul Nzenti, "Petrography and Major Element Geochemistry of the Endengue Iron Formations, Ntem Complex, South Cameroon." *Journal of Geosciences and Geomatics*, vol. 8, no. 1 (2020): 15-24. doi: 10.12691/jgg-8-1-3.

1. Introduction

Iron formations are iron-rich chemically precipitate rocks, typically thin-bedded and/or finely laminated, commonly but not necessarily containing layers of chert with at least 15% iron [1]. They are usually found on Precambrian area generally associated to greenstone belt [2]. The banded iron formations (BIFs) with alternating Fe-rich and Si-rich bands which are the principal sources of iron ore in global steel industries with 90% of iron ore exploitation [3].

In Cameroon, BIFs occur within Archean to early Paleoproterozoic Ntem complex at the NW of Congo craton. This complex hosts many BIF-hosted iron ore deposits such as Mballam [4,5], Nkout [6,7], Bikoula [8], Ngovayang [9], Kouambo [10] and Gouap [11] deposits (Figure 1a). Various iron-formation sequences, particularly those of Archean in age, are the metamorphic products of the iron minerals [12]. Previous studies have revealed that the Ntem Complex BIFs have been metamorphosed to various grade, ranging from greenschist to granulite facies metamorphism [6,10,11]. As result, most BIFs appear as magnetite quartzite and where the metamorphic grade was high (upper amphibolite to granutlite facies), as magnetite gneiss. In the Endengue area, metamorphosed iron formations have been recently discovered and no data are yet available on these formations. In this paper, we report the first detailed petrographical and whole rock geochemical data of the Endengue magnetite gneiss with the aim to discuss the origin and the iron ore potential of these rocks.

2. Geological Setting

The Endengue area lies within the Archean Ntem unit which belongs to the Ntem Complex greenstones belt at

the northwestern edge of the Congo Craton in southern Cameroon (Figure 1b). The Congo craton is a vast Archean (> 2.5 Ga) unit which includes the Bangweulu block in Zambia; the Tanzanian craton, the Kasaï Angola and Congo Democratic Republic (CDR) block, the Tete block; the Chaillu craton in Gabon and Congo, the Bomu-Kibalien block extending in Congo, CAR (Central Africa Republic) and CDR and the Ntem complex in Cameroon [14,15]. The Ntem complex is characterized by two orogenic cycles. The first cycle corresponds to Liberian orogeny and is marked by the formation of greenstone belt, followed by the intrusion of TTG (tonalite, trondhjemite, granodiorite) between 2900 and 2800 Ma. This cycle is ended by the anatectic potassic granitoid intrusion between 2600 and 2500 Ma [16,17]. The second cycle comprises metasedimentary and metaigneous rocks form during the Eburnean high-grade tectono-metamorphic event. This event is marked by the intrusion of alkali syenite at ca 2300 Ma follow with the emplacement of doleritic dykes at 2100 Ma and the amphibolite to granulite facies metamorphism at 2050 [18,19,20,21]. Zircon U-Pb ages and Hf-O isotopes data from the Ntem unit reveals that the charnockites crystallized at ca. 2.92 Ga while the trondhjemites and associated amphibolite protoliths crystallized synchronously at around 2.87-2.86 Ga [22]. Recent works in this unit have reported the existence of well-preserved eclogites and serpentinized peridotites interpreted as related to supra subduction zone setting [23,24,25].

3. Sampling and Analytical Methods

For this study, twelve fresh representative samples of magnetite gneiss were selected for both petrographical and geochemical studies. Sampling location sites are shown in Figure 1b. Polished thin sections were prepared at the Geotech Lab, Vancouver (Canada) using conventional techniques. Textural and mineralogical studies of these samples were carried out using optical microscopy at the University of Yaoundé I, Cameroon. Whole rock geochemical analysis was performed using the pulp by Inductively Coupled Plasma-Atomic Emission (ICP-AES) for major elements at ALS Minerals Global Group, Vancouver (Canada). The samples were pulverized to obtain a homogeneous sample out of which 50-60 g was obtained for the analyses, 0.2 g of rock powder was fused with 1.5 g LiBO2 and then dissolved in 100 mm 35% HNO_3. Analytical uncertainties vary from 0.1% to 0.04% for major elements. Loss on ignition (LOI) was determined by weight difference after ignition at 1000°C. Various standards were used and data quality assurance was verified by running these standards between samples as unknowns.

4. Results

4.1. Petrography

The Endengue IFs are associated to biotite-pyroxene gneiss, biotite granite and charnockite (Figure 1b). They crop as flagstone (Figure 2a), dark gray to yellowish in color when and display finely alternation of light quartzo-feldspathic bands and dark iron-rich bands (Figure 2b). Under transmitted light, the magnetite gneiss displays a heterogranular granoblastic microstructure composed of quartz (33-40%), magnetite (30-38%), pyroxene (10-15%), amphibole (6-15%), plagioclase (5-12%) and secondary goethite (2-5%) (Figure 2c). Quartz is the most abundant mineral of the rock. It appears as subhedral to euhedral crystals forming silica-rich layers. Some quartz crystals are as inclusions in magnetite. Magnetite occurs as euhedral to anhedral crystals, 0.2 to 1.7 mm in size, disseminated within the rock, and sometimes associated with pyroxene and goethite (Figure 2d). Hydratation to goethite is common in the weathered samples (Figure 2e). Orthopyroxene appears as subhedral to euhedral crystals, < 1 mm in size, associated with plagioclase and magnetite (Figure 2c, d and f). Some pyroxene crystals show conspicuous transformation to magnetite. Amphibole crystals green in color, euhedral in shape. They are secondary minerals and represent the alteration products of pyroxene. Apatite and allanite are accessory mineral phases.

Biotite-pyroxene gneiss are gray-dark in color and crop as flagstones (Figure 3a). Under the microscope, the rock is composed of quartz, potassic feldspar, biotite, plagioclase, pyroxene and opaque minerals and displays a granoblastic microstructure (Figure 3b). Quartz (25-30%) is the most abundant mineral and appears as subhedral to euhedral crystals with variable sizes, ranging between 0.5 and 1 mm. Potassic feldspar (15-20%) crystals are euhedral in shape with grain size up to 1.8 mm and host muscovite flakes inclusions. Some crystals show almond-shape suggesting the mylonitisation effects. Biotite (15-20%) appears as small flakes (< 0.5 mm) frequently found in association with pyroxene and opaque minerals (Figure 3b). Pyroxene (5%) occurs as prisms of variable sizes (0.5 to 1.5 mm), often associated with quartz and opaque crystals (Figure 3b).

Biotite granites are medium to coarse-grained (Figure 3c) and display porphyritic microstructure compose of quartz (35-45%), potassic feldspar (30-40%), biotite (5-10%) and magnetite (<5%) (Figure 3d). Quartz appears as anhedral fine crystals, sometimes encountered as inclusion in K-feldspar crystals. The later occurs as subhedral to euhedral crystals with average grain size of 1.2 mm. Biotite exhibits distinct small flakes, subhedral in shape (Figure 3d). Magnetite minerals are present as anhedral crystals, < 1 mm size associated with biotite (Figure 3d).

Charnockites occur as massive blocks, pink in color and medium to coarse-grained (Figure 3e). The main minerals of this rock are quartz (25-30%), orthopyroxene (15-20%), potassium feldspar (15-20%), plagioclase (5-10%), biotite (3-8%) and magnetite (2%). Quartz occurs as anhedral crystals, 0.3 to 1mm in size, commonly associated to feldspar (Figure 3f). Orthopyroxene appear as large (0.3 to 1.2 mm) prismatic crystals associated with plagioclase and biotite (Figure 3f). Potassium feldspar is present as subhedral and euhedral crystals to up 1 mm in size, sometimes associated to plagioclase and quartz (Figure 3f). Biotite appears as very small crystals (< 0.5 mm in size), associated to the magnetite and orthopyroxene (Figure 3f).

4.2. Major Element Geochemistry

The whole-rock geochemical data of the Endengue IFs

are reported in Table 1. The chemical composition show high Fe_2O_3 and SiO_2 contents, ranging from 51.4 to 62.8 wt-% (average of 58.95 wt-%) and 31.1 to 43.9 wt-% with an average of 34.68 wt-%, respectively. The Al_2O_3 content ranging from 0.21 to 4.5 wt-% (average of 1.95 wt-%) shows slightly enrichment and suggests a detrital contamination during the Edengue IFs deposition. In addition, the average $Al_2O_3 + TiO_2$ content of 2.14 wt-% indicates the contribution of terrigenous clastic material in the studied IFs [27]. Otherwise the low TiO_2 (average of 0.19 wt-%) indicate that the contamination was trivial.

Pearson's inter-elements correlation matrix is presented in Table 2. The strong negative correlation (r= -0.88) between SiO_2 and Fe_2O_3 indicate a reverse distribution of silica and magnetite in the rock. We can notice a weak positive correlation (r= 0.54) between Al_2O_3 and CaO. Indeed, the Al_2O_3 and Fe_2O_3 displays weak negative correlation (r= -0.40), while Al_2O_3 with SiO_2, TiO_2, K_2O, MnO and Cr_2O_3 show weak to strong positive correlation (Table 2). The Endengue IFs show low concentrations of CaO and MgO, ranging from 0.01 to 0.52 wt-% (average of 0.16 wt-%) and 0.04 to 2.58 wt-% (average of 0.77 wt-%) respectively. The strong positive correlation between CaO and MgO (r= 0.80), indicate the mixing of MgO in carbonate [28]. The K_2O and Na_2O contents are strongly depleted in all samples (average =0.07 wt-% and 0.06 wt-%, respectively). MnO and P_2O_5 concentrations (0.04 to 0.14 wt-% average= 0.10 wt-%; 0.02 to 0.012 wt-%, average=0.07 wt-%, respectively) are generally very low in all samples. MnO and Fe_2O_3 show very weak positive correlation (r= 0.01). The LOI content range from -0.45 to 2.46 wt-%.

The Si/Al ratio fluctuate between 8.29 and 209.05 (average of 38.69), which is lower than that of other BIFs from the Ntem Complex [28]. On the $CaO+MgO-Fe_2O_{3tot}$-SiO_2 [29] and SiO_2-Al_2O_3-FeO [30] ternary diagrams, the investigated iron formations samples plot in the Precambrian BIFs field (Figure 4), indicating that the major element components of the Endengue IFs are like those other BIFs worldwide.
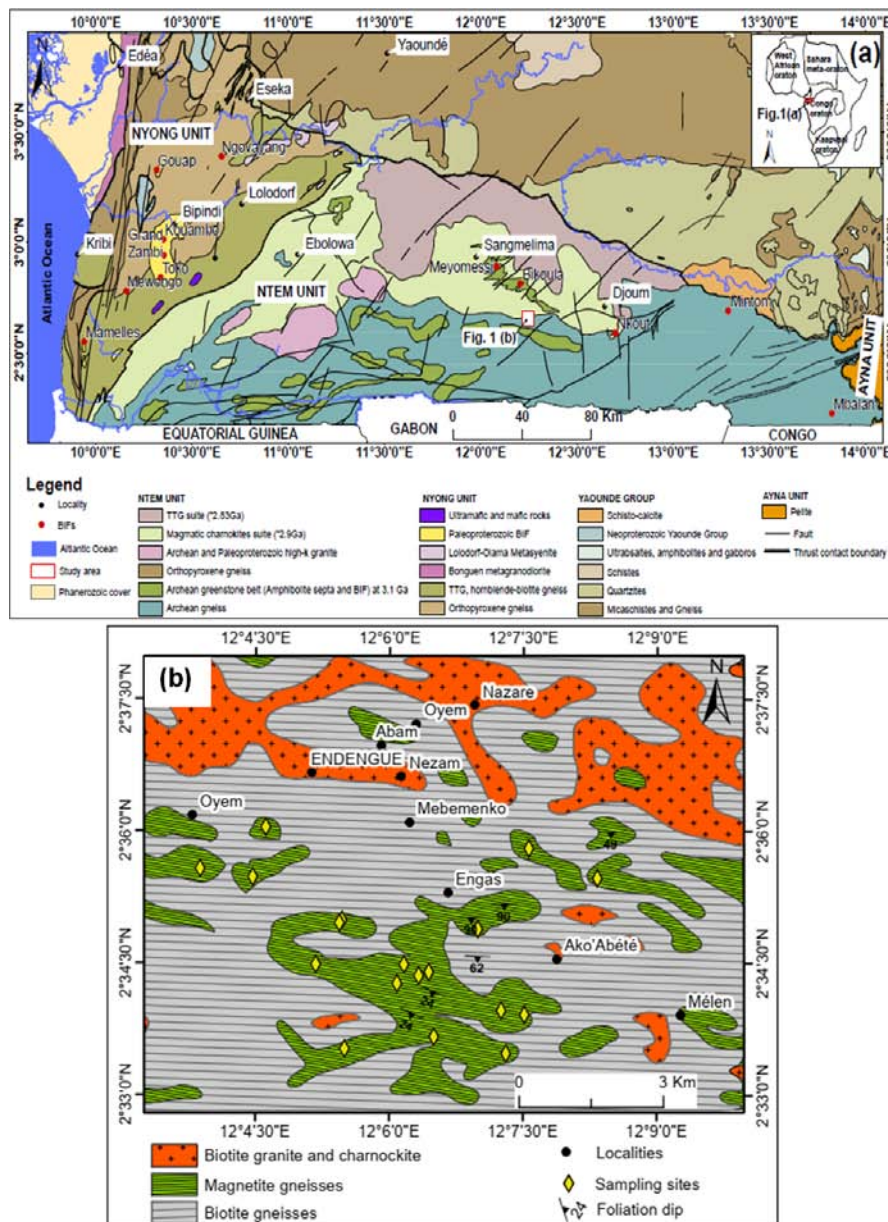

Figure 1. Geological map of SW Cameroon (modified after [13]) showing the Endengue area with some zone of BIFs hosted the Ntem Camplex (a). Geological sketch map of the Endengue area showing samples location (b).
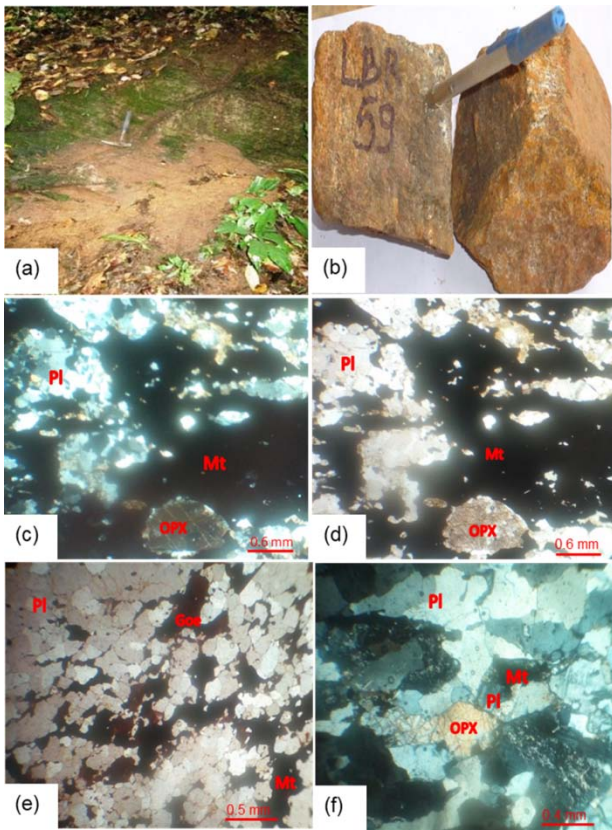
Figure 2. Macroscopic (a-b) and photomicrograph (c-f) views of the studied iron formations. (a) Field exposure and (b) hand specimen's picture showing microbanding; (c-f) Transmitted light photomicrographs showing Opx+Pl+Mt mineral assemblages (c,f); destabilization of pyroxene to magnetite; and red pink coloration of goethite which altered to magnetite (e); l. Opx, orthopyroxene; Pl, plagioclase; Geo, goethite; Mt, magnetite. Mineral abbreviation based on [26]

Figure 3. (a) Exposure of biotite-pyroxene gneiss; (b) coarse grained texture of biotite-pyroxene gneiss consisting of quartz (Qtz), orthopyroxene (Opx), potassic feldspar (Kfs), biotite (Bt), (plane-polarized light); (c) exposure of biotite granite; (d) granular texture of biotite granite showing the mineral composition (plane-polarized light); (e) outcrop view of charnockite; and (f) granoblastic heterogranular texture and mineral composition (plane-polarized light).
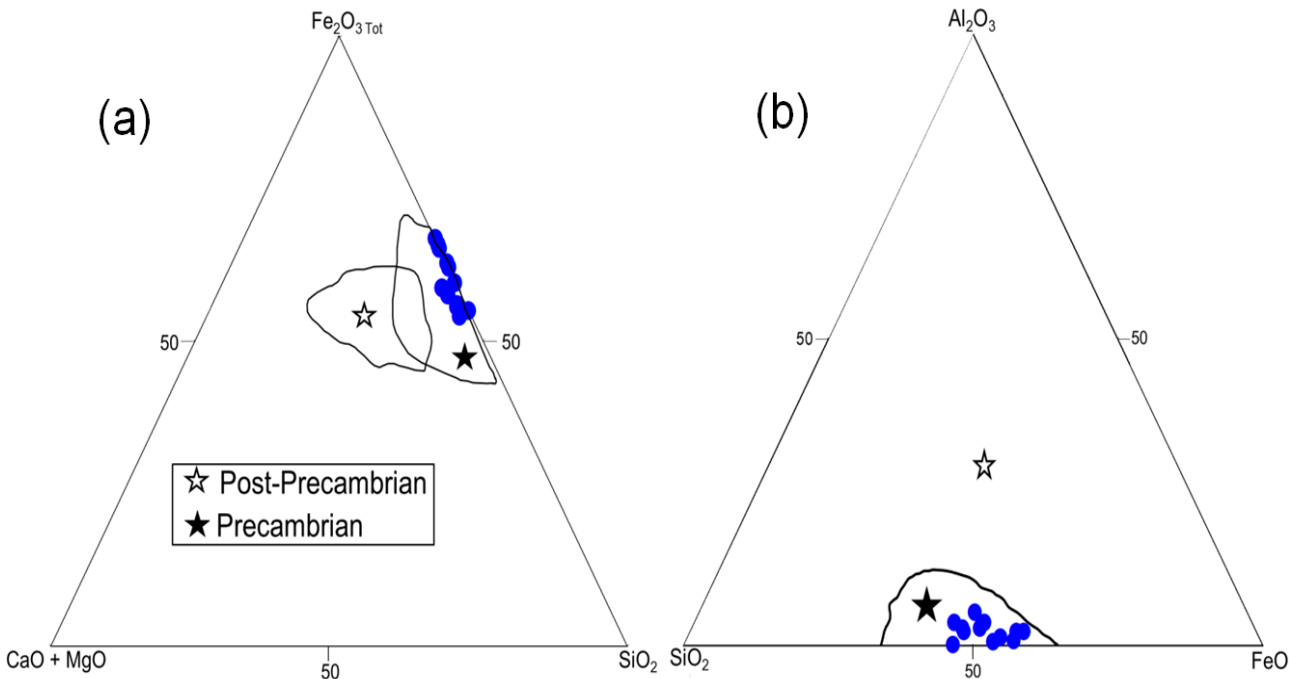

Figure 4. (a) CaO+MgO-Fe$_2$O$_3$Tot-SiO$_2$ [29] and (b) SiO$_2$-Al$_2$O$_3$-FeO [30] ternary diagrams showing the Precambrian age of the Edengue metamorphosed iron formations.

Table 1 Representative major elements composition (wt-%) and element ratios of the Endengue iron formations

Samples	LBR50	LBR51	LBR57A	LBR57B	LBR59A	LBR59B	LBR60	LBR61A	LBR61B	LBR63	LBR65	LBR69	Av.
Weight percent													
SiO_2	37.9	36.4	31.7	31.1	35.1	41.6	43.9	31.4	34.9	40.2	37.3	39.7	36.77
TiO_2	0.17	0.4	0.15	0.15	0.17	0.29	<0.01	0.02	0.02	0.14	0.43	0.18	0.19
Al_2O_3	2.2	3.01	1.82	1.8	1.2	3.11	0.21	0.68	0.62	1.93	4.5	2.33	1.95
Fe_2O_3	56.1	55.7	61.1	62.8	59.5	51.4	53.9	59.1	57.3	53.1	53.5	52	56.29
MnO	0.07	0.14	0.14	0.14	0.08	0.11	0.04	0.05	0.05	0.12	0.17	0.1	0.10
MgO	0.15	2.58	0.07	0.1	0.04	1.64	0.08	0.09	0.08	1.19	1.9	1.36	0.77
CaO	0.02	0.24	0.01	0.02	0.01	0.52	0.01	0.01	0.01	0.44	0.34	0.3	0.16
Na_2O	0.01	0.02	0.01	<0.01	<0.01	0.09	<0.01	<0.01	<0.01	0.07	0.18	0.07	0.06
K_2O	0.1	0.16	0.03	0.03	0.02	0.07	<0.01	0.01	0.02	0.08	0.22	0.04	0.07
P_2O_5	0.11	0.1	0.04	0.02	0.09	0.07	0.05	0.08	0.05	0.12	0.04	0.12	0.07
Cr_2O_3	0.01	0.06	0.03	0.03	0.03	0.04	0.01	0.01	0.01	0.02	0.07	0.01	0.03
Total	98.53	99.26	95.16	95.74	96.23	99.07	98.71	93.91	95.38	97.2	99.13	97.92	97.19
Si/Al	17.23	12.09	17.42	17.28	29.25	13.38	209.05	46.18	56.29	20.83	8.29	17.04	38.69
Al/Ti	12.94	7.53	12.13	12.00	7.06	10.72		34.00	31.00	13.79	10.47	12.94	14.96
Fe/Ti	330.00	139.25	407.33	418.67	350.00	177.24		2955.00	2865.00	379.29	124.42	288.89	766.83
Fe/Al	25.50	18.50	33.57	34.89	49.58	16.53	256.67	86.91	92.42	27.51	11.89	22.32	56.36
Fe/Si	1.48	1.53	1.93	2.02	1.70	1.24	1.23	1.88	1.64	1.32	1.43	1.31	1.56
$Al_2O_3 + TiO_2$	2.37	3.41	3.4	2.07	4.93	2.51	1.97	1.95	1.37		0.7	0.64	2.14
MnO/TFe_2O_3	0.0012	0.0025	0.0021	0.0023	0.0032	0.0019	0.0023	0.0022	0.0013	0.00074	0.00085	0.00087	0.0018

Table 2. Pearson's correlation matrix for major element oxides.

	SiO_2	TiO_2	Al_2O_3	Fe_2O_3	MnO	MgO	CaO	Na_2O	K_2O	P_2O_5	Cr_2O_3	LOI
SiO_2	1											
TiO_2	0.42	1										
Al_2O_3	0.14	**0.93**	1									
Fe_2O_3	**-0.88**	-0.45	-0.40	1								
MnO	-0.18	0.75	0.81	**0.01**	1							
MgO	0.37	0.83	0.79	**-0.63**	0.60	1						
CaO	0.54	0.56	0.68	-0.77	0.49	**0.80**	1					
Na_2O	0.38	0.54	0.80	-0.59	0.52	0.46	0.63	1				
K_2O	0.40	**0.87**	**0.88**	-0.48	0.62	0.76	0.49	0.56	1			
P_2O_5	0.37	-0.01	0.06	-0.48	-0.19	0.31	0.35	-0.37	0.04	1		
Cr_2O_3	-0.06	0.90	0.80	-0.10	0.80	0.71	0.44	0.52	0.78	-0.24	1	
LOI	-0.58	-0.36	-0.27	0.72	-0.15	-0.53	-0.62	-0.57	-0.41	-0.24	-0.15	1

5. Discussion

5.1. Metasomatic Imprints

The Endengue IFs are located within the high grade terrain of the Archean Ntem unit. Their mineral assemblages of orthopyroxene, amphibole and biotite contain key minerals that indicated high grade metamorphic conditions. The presence of apatite as accessory mineral in the investigated rocks, suggests metasomatic alteration. Assuming limited vertical phosphate remobilization during diagenesis, it is likely that the apatite precipitated either as two separate phases, preferentially with primary ferric hydroxides

(now goethite) [31] or it was associated with the organic remains of planktonic bacteria that settled out to the seafloor [32]. The destabilization of magnetite to goethite in the IFs is due to the precipitation of hydrothermal fluids process [33]. In addition, the presence of magnetite can also be explained by conversion of pyroxene to magnetite in the presence of hydrothermal fluid through diagenetic process and/or the conversion of goethite to magnetite. Some iron oxide laminar are derived from abundant hematite and/or goethite particles that were originally encapsulated in chert layers and subsequently liberated by removal of quartz during post-depositional deformation through dissolution and precipitation [34]. The alteration

of orthopyroxene to magnetite observed in the Edengue IFs support the metamorphic and hydrothermal input. In addition, the studied IFs show conspicuous silicification which is attributed to silica overprint from hydrothermal fluids linked to late granitoid emplacement in the study area. Similar metasomatic signatures were observed in the Ngovayang IFs in the northwestern part of the Ntem Complex [9].

5.2. Origin of Chemical Components

Iron formations can be resulted from interaction of shallow seawater, hydrothermal alteration of ocean crust, weathering of continental landmass, mixture of seawater hydrothermal fluids and weathering of continental crustal material [35,36,37]. Due to this complexity, different approaches mainly based on geochemistry, were suggested to investigate the origin of chemical components in IFs. The chemical statistics of the Endengue IFs shows high contents of total $Fe_2O_3 + SiO_2$ (average of 93.06 wt-%), similar to the $TFe_2O_3 + SiO_2$ values of the iron formations in the Ntem Complex [6,9,11,28,38,39], suggesting the purity of the chemical precipitation. Otherwise Al_2O_3 and TiO_2 are used as proxies to quantify clastic input, that should increase the $Al_2O_3 + TiO_2$ concentration up to 2 wt-% in BIFs since they are immobile and cannot be introduced in solution during hydrothermal, diagenetic and weathering processes [27,40]. The average $Al_2O_3 + TiO_2$ content of 2.14 wt-% suggested a significant detrital input during deposition of the Endengue IFs. This clastic involvement is supported by the strong positive correlation between Al_2O_3 and TiO_2 (r= 0.93). Moreover, the strong positive correlation between Al_2O_3 with K_2O, Na_2O, MgO and CaO (Table 2) indicates that terrigenous clastic materials were involved during the deposition of the Endengue IFs which can be present in detrital particles [41,42]. These results are comparable to those obtained in the Bikoula BIFs from the Ntem unit [8] and in the Ngovayang magnetite gneiss in the Nyong unit [9]. However, Ganno et al. [28] have suggested that the Elom BIFs, situated some 10 Km NE of the Endengue area, have recorded trivial detrital input.

According to their resistance and insoluble character, Al^{3+} and Ti^{4+} cations are used to identify the input in hydrothermal fluid and seawater during sedimentation [43,44,45]. Indeed, Si/Al, Fe/Al, and Fe/Ti ratios are high in hydrothermal fluids [11,38]. Therefore, the average Si/Al (38.69); Fe/Ti (766.83); Fe/Al (56.36) ratios of the Endengue IFs are comparable to other BIFs in the Ntem Complex, and indicate the input of hydrothermal derived component during sediments deposition. Wonder et al. [46] have proposed the use of $Al_2O_3 - SiO_2$ diagram to discriminate the origin of BIFs. On this diagram, all the Endengue IFs samples (except LBR65) plot in hydrothermal origin field. The high detrital contaminated sample LBR65 falls on the boundary between the hydrothermal and hydrogenous fields (Figure 5). This result is supported by the Fe-Mn-Al ternary diagram [48], that shown predominant hydrothermal origin of the Endengue IFs (Figure 6) similar to the Mesoarchean Bikoula BIFs [8]. Since Fe_2O_3 and MnO are rich in components of hydrothermal fluids, many authors (eg. [11,44,49]) have proposed that the MnO/Fe_2O_3

ratio in BIFs characterized hydrothermal origin. The MnO/Fe_2O_3 ratio of the Endengue IFs is extremely low (0.07-2.5*10^{-3}; average= 1.8*10^{-3}), when comparable to the Kpwa-Atog Boga BIFs within the Paleoproterozoic Nyong unit [11], suggesting a predominant hydrothermal origin.
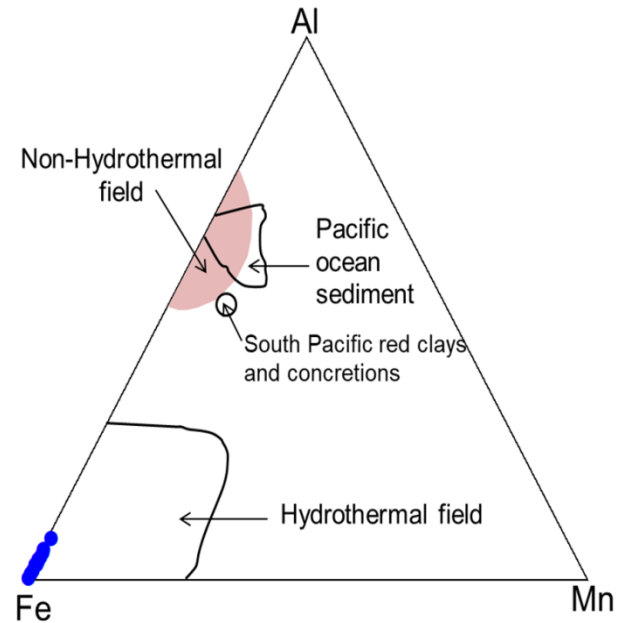

Figure 5. SiO_2 - Al_2O_3 discrimination diagram [47] indicating the hydrothermal affinity of the studied iron formations.

To evaluate the degree of dilution of hydrothermal input by clastic or volcanic detritus, Barrett [50] proposed a plot of Fe/Ti versus Al/(Al+Fe+Mn). The studied IF samples plot closer the hydrothermal Red Sea deposits and East Pacific Rise deposits, very far from the field of modern pelagic terrigenous sediments (Figure 7). From the above discussion, it can be suggested that the major components (> 80%) of the Endengue IFs are predominantly hydrothermal in origin.
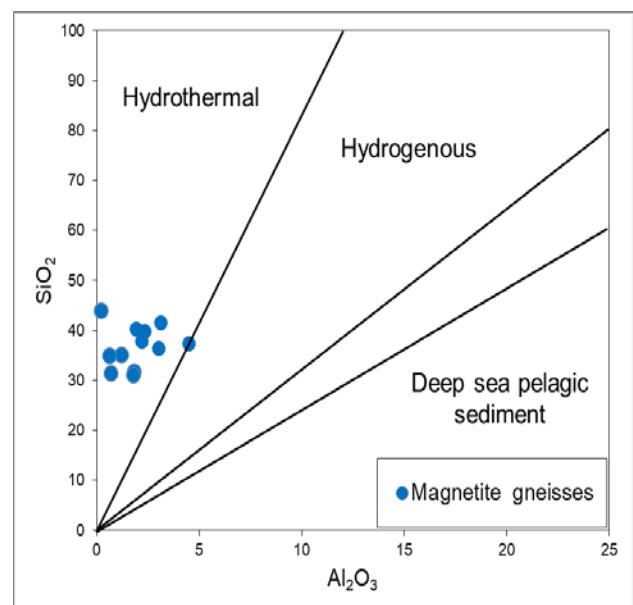

Figure 6. Ternary Fe-Mn-Al plot showing hydrothermal and non-hydrothermal fields for modern marine ferromanganese deposits [48].
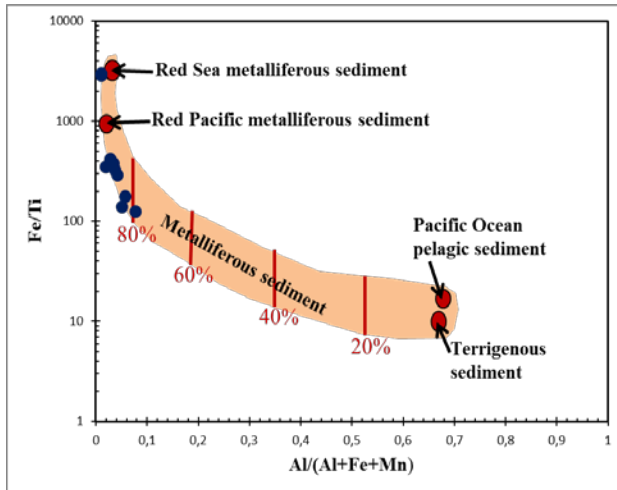
Figure 7. Fe/Ti versus Al/ (Al + Fe + Mn) discrimination diagram indicating the hydrothermal affinity of the studied iron formations. The curve represents mixing of East Pacific Rise deposits (EPR) with pelagic sediments (PC). Whereas the numbers indicate the approximate percentage of EPR in the mixture (adopted from [50]).

5.3. Classification of Ore Types

An ore is a natural occurrence of rock or sediment that contains sufficient minerals with economically important elements, typically metals [51,52]. The geological literature comprises several schemes for classifying ore minerals. Clout and Manuel [53] classified iron ore in "ore group" related with the dominant mineral type, hardness, and texture. Moreover, there is no specific classification of iron ores based on their grade in fact that the price of iron is not standard. Based on the Fe_2O_3 concentration, exploited iron ores can be classified into three basic classes: (i) high-grade iron ores with a TFe_2O_3 content above 65 wt-%; (ii) medium-grade ores with Fe_2O_3 concentration fluctuated between 52 and 65 wt-%; and (iii) low-grade ores with Fe_2O_3 values 52 wt-% [54].

The petrography studies of the Endengue magnetite gneiss have shown that they are well foliated and coarse-grained; hard; slightly weathered; dominated by quartz, magnetite and goethite. The major ore mineral (magnetite) is coarse grained and has a granoblastic heterogrnular texture. The geochemical statistic of the studied iron samples reveals the high content of Fe and Si which represent more than 96 wt-% of the average composition. Furthermore, the TFe_3 concentration which range from 35.98 to 43.96 wt-% (average of 39.40 wt-%)

corresponds the low-grade iron ores by global standards [54]. Guider [55] and Dobbins and Burnet [56] proposed the tolerable concentration of deleterious elements (P and S) in the commercial iron ore should be lower than 0.07wt-% P and 0.1wt-% S respectively. The studied IF samples have low gangue (34.68 wt-% SiO_2 and 1.055 wt-% Al_2O_3) and deleterious (P: 0.07 wt-%) elements concentration.

To determine the origin of ore type, Angerer et al. [57] have suggested the use of the whole-rock geochemical data of the iron ore and proposed the SiO_2/Fe_2O_3 and $(MgO + CaO + MnO)/Fe_2O_3$ discrimination diagram. Consequently, the higher $(Mg + Ca + Mn)/Fe$ and lower Si/Fe ratios reveal carbonate-silicate metasomatism and the decrease in the Si/Fe and $(Mg + Ca + Mn)/Fe$ ratios of the high-grade magnetite-hematite-goethite ores in all high-grade ore deposits worldwide. Moreover, this diagram highlights the ratio between primarily dominant silica and additional elements through carbonate-silicate alteration (mainly Mg, Ca, Mn) and hence differentiates unaltered siliceous BIF from BIF that was likely hypogene-altered and associated hypogene ore [57]. In this diagram most of the investigated samples plots in the field of medium-grade siliceous ore and four samples (LBR59, LBR 63, LBR 65 and LBR 69) fall in the low-grade siliceous BIFs field (Figure 7). This suggests that the Edengue IFs can be classified as low grade siliceous ore deriving from the BIF protore.

5.4. Comparative Study

A comparison of the major element composition of Endengue IFs with Ngovayang IFs and BIFs from other parts of the Ntem Complex has revealed a nearer chemical similarity with other Precambrian BIFs worldwide (Table 3). The average concentration of Na_2O, K_2O, TiO_2 and P_2O_5 of the Endengue IF samples show close pattern with the Elom BIFs situated some 10 Km North of the studied area (Figure 9). The Al_2O_3, K_2O, Na_2O, CaO, MgO and P_2O_5 contents are depleted in Endengue IFs but high than the Elom BIFs. MgO and CaO are depleted in Endengue iron deposit than the Ngovayang IFs within the Nyong unit. The Al_2O_3 content is high in the Um Anab (Egypt) IFs, Bikoula BIFs and Ngovayang IFs than Endengue magnetite gneiss but lower in the Jerome (USA) IFs and Nkout BIFs. Additionally, the studied IFs display high Fe_2O_3 content when compare with the global Superior BIFs and Algoma BIFs (Figure 9).

Table 3. Comparison of the study area major element (wt-%) with IF and BIF types areas of the world

Location	This study	Ngovayang IF[a]	Elom BIF[b]	Bikoula BIF[c]	Nkout BIF[d]	Um Anab (Egypt) IF[e]	Jerome (USA) IF[f]	Algoma BIF[g]	Superior BIF[h]
SiO_2	36.77	46.84	39.98	37.77	40.12	54.62	18.16	50.5	47.2
TiO_2	0.19	0.51	0.03	0.36	0.03	0.2	0.04	/	/
Al_2O_3	1.95	3.76	0.48	2.88	0.83	3.6	1.04	3	1.39
Fe_2O_3	56.29	43.68	58.19	49.97	53.88	35.14	77.78	41.33	44.51
MnO	0.10	0.07	0.07	0.48	0.09	0.07	0.13	0.22	0.73
MgO	0.77	2.69	0.06	4.44	2.61	1.28	0.09	1.53	1.24
CaO	0.16	1.49	0.02	3.15	1.07	2.98	0.92	1.51	1.58
Na_2O	0.06	0.28	0.01	0.85	0.1	0.25	0.09	0.31	0.12
K_2O	0.07	1.08	0.02	0.76	0.26	0.12	0.22	0.58	0.14
P_2O_5	0.07	0.24	0.08	0.11	0.08	0.54	/	0.21	0.06

a- Chombong et al. [9], b- Ganno et al. [28], c- Teutsong et al. [8], d- Ndime et al. [6], e and f- Li et al. [58], g and h- Prasad et al. [59].
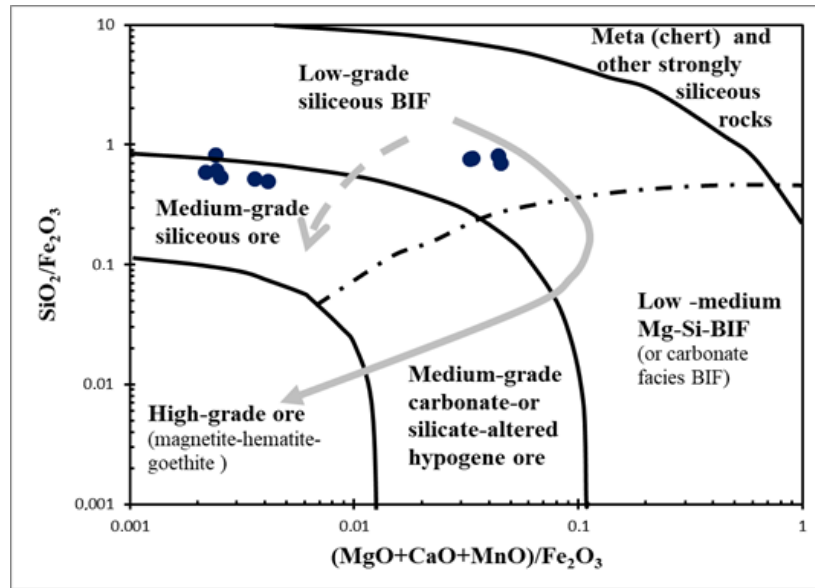
Figure 8. Whole-rock (MgO + CaO + MnO)/Fe_2O_3total versus SiO_2/Fe_2O_3total discrimination diagram [57] depicting the low to medium-grade ore types of the Endengue IFs. Discrimination fields and arrows showing alteration trends including MgO + CaO + MnO-rich (solid arrow) and -poor (dash arrow) stages.
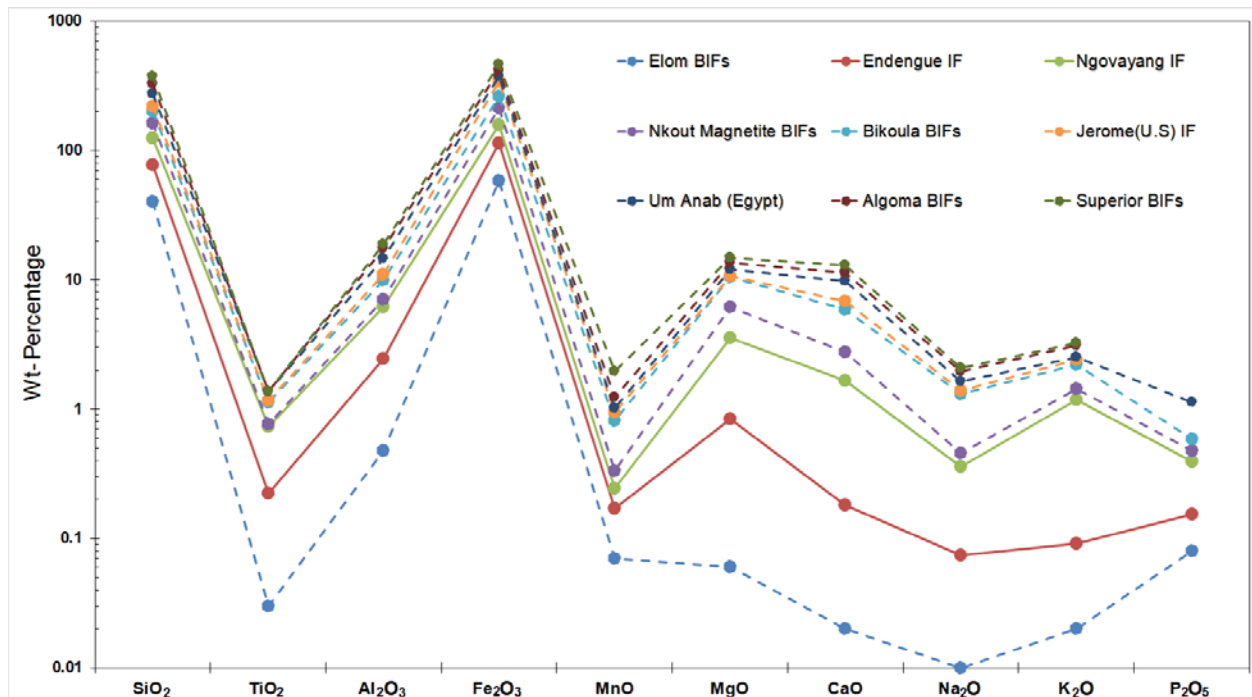

Figure 9. Variation in major element chemical composition of Endengue IFs in relation with other Precambrian IFs in Cameroon and worldwide

6. Conclusion

The petrographical and geochemical analysis of the Endengue IFs has directed to the following conclusions:

(1) The IF samples are hard, finely banded and composed of magnetite, pyroxene, quartz and goethite. Goethite is the secondary mineral, resulting in the hydration of magnetite due to supergene alteration.

(2) Whole-rock composition of the studied IFs reveals that iron and silica are the main constituents (average Fe_2O_3 + SiO_2 of 93.06 wt-%), suggesting the purity of the chemical precipitation.

(3) Their high Si/Al, Fe/Al, Fe/Ti, and low Fe_2O_3/MnO ratios are consistent with a predominantly hydrothermal origin.

(4) The average TFe content of 39.40 wt-%, low gangue (34.68 wt-% SiO_2 and 1.05 wt-% Al_2O_3) and deleterious (P_2O_5: 0.07 wt-%) elements contents correspond to accepted commercial low grade siliceous ore by global standards

(5) The Edengue IFs shared chemical similarities with other Precambrian IFs worldwide.

Acknowledgements

References

[1] James, H.L., Sedimentary facies of iron-formations, Econ. Geol. 49 (1954), 235-293.

[2] Clout, J.M.F., Simonson, B.M., Precambrian iron formations and iron-formation hosted iron ore deposits, Economic Geology, 100th anniversary (2005), 643-679.

[3] Ghosh, R., Baidya, T.K., Mesoarchean BIF and iron ores of the Badampahar greenstone belt. Iron Ore Group, East Indian Shield, Journal of Asian Earth Sciences 150 (2017), 25-44.

[4] Suh, C.E., Cabral, A., Shemang, E.M., Mbinkar, L. and Mboudou, G. G. M., Two contrasting iron-ore deposits in the Precambrian mineral belt of Cameroon, West Africa, Explor. Min. Geol. 17 (2008), 197-207.

[5] Chombong, N.N., Suh, C.E., 2883 Ma commencement of BIF deposition at the northern edge of Congo craton, southern Cameroon: new zircon SHRIMP data constraint from metavolcanics, Episodes 36 (2013) 47-57.

[6] Ndime, E.N., Ganno, S., Soh, Tamehe, L., Nzenti, J.P., Petrography, lithostratigraphy and major element geochemistry of Mesoarchean metamorphosed banded iron formation-hosted Nkout iron ore deposit, north western Congo craton, Central West Africa, J. Afr. Earth Sci. 148 (2018), 80-98.

[7] Ndime, E.N., Ganno, S., Nzenti, J.P., Geochemistry and Pb-Pb geochronology of the Neoarchean Nkout West metamorphosed banded iron formation, southern Cameroon, International Journal of Earth Sciences 108 (2019), 1551-1570.

[8] Teutsong, T., Bontognali, T.R.R., Ndjigui, P.D., Vrijmoed, J.C., Teagle, D., Cooper, M. and Vance, D., Petrography and geochemistry of the Mesoarchean Bikoula banded iron formation in the Ntem complex (Congo craton), southern Cameroon: Implications for its origin, Ore Geology Reviews 80 (2017), 267-288.

[9] Chombong, N.N., Suh, C.E., Lehmann, Vishiti, B., Ilouga, A., Shemang, D.C., Tantoh, E. M., & Kedia A.C., Host rock geochemistry texture and chemical composition of magnetite in iron ore in the Neoarchaean Nyong unit in southern Cameroon, Applied Earth Science (2017).

[10] Ganno, S., Njiosseu, T.E.L., Kouankap, N.G.D., Djoukouo, S.A.P., Moudioh, C., Ngnotué, T. and Nzenti. J.P., A mixed seawater and hydrothermal origin of superior-type banded iron formation (BIF)-hosted Kouambo iron deposit, Palaeoproterozoic Nyong series, southwestern Cameroon: Constraints from petrography and geochemistry, Ore Geology Reviews 80 (2017), 860-875.

[11] Soh, T.L., Tankwa, M.N., Chongtao, W., Ganno, S., Ngnotue, T., Kouankap, N.G.D., Shaamu, J. S., Zhang, J., Nzenti, J.P., Geology and geochemical constrains on the origin and depositional setting of the Kpwa-Atog Boga banded iron formations (BIFs), northwestern Congo craton, southern Cameroon, Ore Geology Reviews 95 (2018), 620-638.

[12] Klein, C., Some Precambrian banded iron-formations (BIFs) from around the world: Their age, geologic setting, mineralogy, metamorphism, geochemistry, and origin, American Mineralogist 90 (2005), 1473-1499.

[13] Maurizot, P., Abessolo, A., Feybesse, J.L., and Johan, L.P., Étude de prospection minière du Sud-Ouest Cameroun, Synthèse des travaux de 1978 à 1985, Rapport de BRGM 85 (1986), 274.

[14] Boillot, G., Huchon, P., Lagabrielle, Y., Boutler, J., Introduction à la géologie, La dynamique de la Terre, Dunod (2008), 74-80.

[15] Kusky, M.T., Li, X., Wang, Z., Fu, J., Ze, L., Zhu, P., « Are Wilson Cycles preserved in Archean cratons? A comparison of the North China and Slave cratons », Canadian Journal of Earth Sciences 51(3) (2013), 297-311.

[16] Toteu, S.F., Penaye, J., Poudjom Djomani, Y.H., Geodynamic evolution of the Pan-African belt in Central Africa with special reference to Cameroon, Canadian Journal of Earth Sciences 41 (2004), 73-85.

[17] Shang, C.K., Liégeois, J.P., Satir, M., Frisch, W., Nsifa, E.N., Late Archean high-K granite geochronology of the northern metacratonic margin of the Archean Congo Craton, Southern Cameroon: evidence for Pb-loss due to non-metamorphic causes, Gondwana Research 475 (2010),1-19.

[18] Van Schmus, W.R., and Toteu, S.F., Were the Congo craton and the Sào Francisco craton joined during the fusion of Gondwanaland? Eostrans AGU, 73(14), Spring Meeting, Supplement 365 (1992).

[19] Tchameni, R., Mezger, K., Nsifa, N.E., and Pouclet, A., Crustal origin of Early Proterozoic syenites in the Congo Craton (Ntem Complex), South Cameroon, Lithos, 57 (1) (2001), 23-42.

[20] Lerouge, C., Cocherie, A., Toteu, S.F., Milesi, J.P., Penaye, J., Tchameni, R., Nsifa, N.E., Fanning, C.M., Shrimp U/Pb zircon age evidence for paleoproterozoic sedimentation and 2.05 Ga syntectonic plutonism in the Nyong Group, South-western Cameroon: consequences for the eburnean-transamazonian belt of NE Brazil and central Africa. Journal of African Earth Sciences 44 (2006), 413-427.

[21] Shang, C.K., Satir, M., Nsifa, E.N., Liégeois, J.P., Siebel, W., Taubald, H., Archaean high-k granitoids produced by remelting of earlier Tonalite-Trondhjemite-Granodiorite (TTG) in the Sangmelima region of the Ntem complex of the Congo craton, southern Cameroon. International Journal of Earth Sciences 96 (2007), 817-841.

[22] Li, X-H., Chen, Y., Li, J., Yang, C., Ling, X-X., Tchouankoue, J.P., New isotopic constraints on age and origin of Mesoarchean charnockite, trondhjemite and amphibolite in the Ntem Complex of NW Congo Craton, southern Cameroon. Precambrian Research 276 (2016), 14-23.

[23] Loose, D., Schenk, V., 2.09 Ga old eclogites in the Eburnian-Transamazonian orogen of southern Cameroon: significance for Palaeoproterozoic plate tectonics. Precambrian Research 304 (2018), 1-11.

[24] Bouyo Houketchang M, Penaye J, Mouri H, Toteu S.F., Eclogite facies metabasites from the Paleoproterozoic Nyong Group, SW Cameroon: mineralogical evidence and implications for a highpressure metamorphism related to a subduction zone at the NW margin of the Archean Congo craton, Journal of African Earth Sciences 149 (2019), 215-234.

[25] Nga, Essomba, T.P., Ganno, S. Tanko, J.E.L., Ndema, Mbongue, M.J.L., Kamguia, W.B., Takodjou, W.J.D., Nzenti, J.P., Geochemical constraints on the origin and tectonic setting of the serpentinized peridotites from the Paleoproterozoic Nyong series, Eseka area, SW Cameroon, Acta Geochemica (2019).

[26] Whitney, D.L., Evans, B.W., Abbreviations for names of rock-forming minerals, American Mineralogist 95 (2010), 185-187.

[27] Kato, Y., Kawakami, T., Kano, T., Kunugiza, K. And Swamy, N.S., Rare-earth element geochemistry of banded iron formations and associated amphibolite from the Sargur belts, south India, Journal Asian Earth Sciences 14 (1996), 161-164.

[28] Ganno, S., Ngnotue, T., Kouankap, N.G.D., Nzenti, J.P., Notsa, F.M., Petrology and geochemistry of the banded iron-formations from Ntem complex greenstones belt, Elom area, southern Cameroon: Implications for the origin and depositional environment, Chemie der Erde - Geochemistry 75 (2015), 375-387.

[29] Lepp, H. and Goldich, S.S., Origin of the Precambrian Iron-Formation, Economic Geology 59 (1964), 1025-1060.

[30] Govett G.J.S., Origin of banded iron-formation; Geological Society of America Bulletin 77 (1966), 1191-1212.

[31] Bjerrum, C.J., & Canfield, D.E., Ocean productivity before about 1.9 Gyr ago limited by phosphorus adsorption onto iron oxides, Nature, 417 (2002), 159-162.

[32] Konhauser, K., Hamade, T., Raiswell, R., Morris, R., Ferris, F., Southan, G., Canfield, D., Could bacteria have formed the Precambrian banded iron formation?, Geology 30 (2002), 1079-1082.

[33] Pecoits, E., Gingras, M.K., Barley, M.E., Kappler A., Posth, N.R., Konhauser, K.O., Petrography and geochemistry of the Dales Gorge banded iron formation: paragenetic sequence, source and implications for palaeo-ocean chemistry, Precambrian Research, 172 (2009), 163-187.

[34] Egglseder, M.S., Cruden, A.R., Tomkins, A.G., Wilson, S.A., Langendam, A.D. Colloidal origin of microbands in banded iron formations, Geochemical Perspectives Letters, 6 (2018), 43-49.

[35] Hamade, T., Konhauser, K.O., Raiswell, R., Goldsmith, S., Morris, R.C., Using Ge/Si ratios to decouple iron and silica fluxes in Precambrian banded iron formations, Geology 31 (2003), 35-38.

[36] Frei, R., Polat, A., Source heterogeneity for the major components of 3.7 Ga banded iron formation (Isua Greenstone Belt, western Greenland): tracing the nature of interacting water masses in BIF formation, Earth and Planetary Sciences Letters 253 (2007), 266-281.

[37] Bekker, A., Slack, J.F., Planavsky, N., Krapez, B., Hofmann, A., Konhauser, K.O., Rouxel, O.J., Iron formation: the sedimentary product of a complex interplay among mantle, tectonic, oceanic and biospheric processes, Economic Geology 105 (2010), 467-508.

[38] Ganno, S., Tsozué, D., Kouankap, N.G.D., Tchouatcha, M.S., Ngnotué, T., Gamgne Takam, R., Nzenti. J.P., Geochemical Constraints on the Origin of Banded Iron Formation-Hosted Iron Ore from the Archaean Ntem Complex (Congo Craton) in the Meyomessi Area. Southern Cameroon, Resource Geology 68(3) (2018), 287-302.

[39] Soh, Tamehe, L., Wei, C.T., Ganno, S., Simon, S.J., Kouankap, Nono, G.D., Nzenti, J.P., Lemdjou, Y.B., Lin N.H., 2019. Geology of the Gouap iron deposit, Congo craton, southern Cameroon: implications for iron ore exploration, Ore Geology Reviews 107 (2018), 1097-1128.

[40] Ewers, W.E., Morris R.C. Studies of the Dales Gorge Member of the Brockman Iron Formation, Western Australia, Economic Geology 76 (1981), 1929-1953.

[41] Klein, C., and Beukes, N.J., Proterozoic iron-formations, In: Condie K.C., (ed) Proterozoic crustal evolution. Elsevier, Amsterdam (1992), 383-418.

[42] Manikyamba, C., and Naqvi, S.M., Geochemistry of Fe-Mn formations of Archaean Sandurschist belt, India: mixing of clastic and chemical processes at a shallow shelf, Precambrian Research, 72 (1995), 69-95p.

[43] Böstrom, K., Submarine volcanism as a source for iron, Earth and Planetary Sciences Letters 9 (1970), (4), 348-354.

[44] Gurvich, E.G., Metalliferous Sediments of the World Ocean: Fundamental Theory of Deep-Sea Hydrothermal Sedimentation, Springer Berlin (2006), 416p.

[45] Cox, G.M., Halverson, G.P., Minarik, W.G., Heron, D.P.L., Macdonald, F.A., Bellefroid, E.J., Strauss, J.V., Neoproterozoic iron formation: an evaluation of its temporal, environmental and tectonic significance, Chemical Geology 362 (2013), 232-249.

[46] Wonder, J., Spry, P., Windom, K., Geochemistry and origin of manganese-rich rocks related to iron-formation and sulfide deposits, western Georgia, Economic Geology 83 (5) (1988), 1070-1081.

[47] Bonatti, E., Metallogenesis at oceanic spreading centers, Annual Reviews Earth and Planetary Sciences 3 (1975), 401-433.

[48] Bostrom, K., The origin and fate of ferromanganoan active ridge sediments, Stockholm Contribution of Geology 27 (1973), 149-243.

[49] Sugitani, K., Geochemical characteristics of Archean cherts and other sedimentary rocks in the Pilbara Block, Western Australia: evidence for Archean seawater enriched in hydrothermally-derived iron and silica, Precambrian Research 57 (1992), 21-47.

[50] Barrett, T.J., Chemistry and mineralogy of Jurassic bedded chert overlying ophiolites in the north Appenines, Italy, Chemical Geology 34 (1981), 289-317.

[51] Freeman, W.H., Physical Description XIV, Illustrated 4th Edition, Published New York. (1986), ISBN 0-7167-1456-6.

[52] Guilbert, J.M., Charles, F., Park, J., The geology of ore deposits, English, Book, Illustrated edition (1986), https://trove.nla.gov.au/version/22205693.

[53] Clout, J.M.F., Manuel, J.R., Mineralogical, chemical, and physical characteristics of iron ore, Iron Ore (2015), http://dx.doi.org/10.1016/B978-1-78242-156-6.00002-2.

[54] Belevtsev, Y.N., Kravchenko. V.M., Kulik, D.A., Belevtsev, Borisenko, R.Y., Drozdovskaya, V.G., Epatko, A.A., Zankevich, Y.M., Kalinichenko, B.A., Koval, O.A., Korzhnev, V.B., Kusheyev, M.N., Lazurenko, V.V., Litvinskaya. M.A., Nikolayenko. V.I., Pirogov. B.I., Prozhogin. L.G., Pikovskiy. V.I., Samsonov, E.S., Skvortsov, V.A., Savchenko, V.V., Stebnovskaya, L.T., Tereshchenko, Y.M., Chaykin, S.I., Yaroshchuk, M.A., Precambrian banded iron formations of the European part of the USSR, Genesis of iron-ores, Naukova Dumka Press, Kiev, Ukrainia (1991), (IGCP UNESCO Project. No 247 (in Russian)).

[55] Guider, J.W., Iron ore beneficiation -key to modern steelmaking, Mineral Engineering 33 (1981), 410-413.

[56] Dobbins, M.S. and Burnet, G., Production of an iron ore concentrate from the iron-rich fraction of power plant fly ash, Resource Conservation 9 (1982), 231-242.

[57] Angerer, T., Hagemann, S.G., Danyushevsky, L.V., Geochemical evolution of the banded iron formation-hosted high-grade iron ore system in the Koolyanobbing Greenstone Belt, Western Australia, Economic Geology 107 (2012), 599-644.

[58] Li, Z.Q., Zhang, L.C., Xue, C.J., Zheng, M.T., Zhu, M.T., Robbins, L.J., Konhauser, K. O., Earth's youngest banded iron formation implies ferruginous conditions in the Early Cambrian ocean. Scientific Reports 8(1) (2018).

[59] Prasad, K.S.S., Sankar D.B., Reddy Y.V., Geochemistry and origin of banded iron-formation from the granulitic terrain of North Arcot District, Tamil Nadu, South India, Chemical Sciences Transaction 1(3) (2012), 482-493.